Global invariant manifolds in the transition to preturbulence in the Lorenz system

Eusebius J. Doedel[a], Bernd Krauskopf[b], Hinke M. Osinga[b]

[a]*Department of Computer Science, Concordia University, 1455 Boulevard de Maisonneuve O., Montréal, Québec H3G 1M8, Canada*
[b]*Bristol Centre for Applied Nonlinear Mathematics, Department of Engineering Mathematics, University of Bristol, Bristol BS8 1TR, United Kingdom*

In memory of Floris Takens

Abstract

We consider the homoclinic bifurcation of the Lorenz system, where two primary periodic orbits of saddle type bifurcate from a symmetric pair of homoclinic loops. The two secondary equilibria of the Lorenz system remain the only attractors before and after this bifurcation, but a chaotic saddle is created in a tubular neighbourhood of the two homoclinic loops. This invariant hyperbolic set gives rise to preturbulence, which is characterised by the presence of arbitrarily long transients.

In this paper we show how and where preturbulence arises in the three-dimensional phase space. To this end, we consider how the relevant two-dimensional invariant manifolds — the stable manifolds of the origin and of the primary periodic orbits — organise the phase space of the Lorenz system. More specifically, by means of recently developed and very robust numerical methods, we study how these manifolds intersect a suitable sphere in phase space. In this way, we show how the basins of attraction of the two attracting equilibria change topologically in the homoclinic bifurcation. More specifically, we characterise preturbulence in terms of the accessible boundary between the two basins, which accumulate on each other in a Cantor structure.

Keywords: Lorenz system, homoclinic explosion, invariant manifolds, preturbulence, Cantor structure.

1. Introduction

Our object of study is the Lorenz system [29]

$$\left\{\begin{array}{rcl} \dot{x} &=& \sigma(y-x), \\ \dot{y} &=& \varrho x - y - xz, \\ \dot{z} &=& xy - \beta z, \end{array}\right. \tag{1}$$

which is arguably the best known continuous-time dynamical system that features chaotic dynamics; see, for example, [3, 13, 42] and references therein. We keep the parameters σ and β fixed at their classical values of $\sigma = 10$ and $\beta = 8/3$, while ϱ acts as the bifurcation parameter. The origin $\mathbf{0}$ of (1) is always an equilibrium; it is stable for $\varrho < 1$ and becomes a saddle point (in a pitchfork bifurcation) at $\varrho = 1$. For $\varrho > 1$ the origin $\mathbf{0}$ has a one-dimensional unstable manifold $W^u(\mathbf{0})$ and a two-dimensional stable manifold $W^s(\mathbf{0})$; throughout we refer to $W^s(\mathbf{0})$ as the Lorenz manifold. There is a considerable difference in magnitude between the two stable real eigenvalues, and we also consider the one-dimensional strong stable manifold $W^{ss}(\mathbf{0}) \subset W^s(\mathbf{0})$. For $\varrho > 1$ there are also the secondary equilibria

$$p^{\pm} = \left(\pm\sqrt{\beta(\varrho-1)}, \pm\sqrt{\beta(\varrho-1)}, \varrho - 1\right),$$

which are each other's image under the symmetry transformation

$$(x, y, z) \mapsto (-x, -y, z) \tag{2}$$

of (1). After they are born in the pitchfork bifurcation at $\varrho = 1$, the equilibria $p^{\pm}$ are attractors with a one-dimensional strong stable manifold $W^{ss}(p^{\pm})$ and a pair of complex conjugate (weaker) stable eigenvalues. The secondary equilibria $p^{\pm}$ lose stability in a subcritical Hopf bifurcation at

$$\varrho_H = \frac{\sigma\,(\beta + \sigma + 3)}{\sigma - \beta - 1} = \frac{470}{19} \approx 24.7368,$$

where they become saddle foci.

We focus on the transition through the first homoclinic bifurcation as the parameter ϱ is increased through $\varrho = \varrho_{\mathrm{hom}} \approx 13.9265$, and how this affects the basins of attraction $\mathcal{B}(p^{\pm})$ of the two attractors $p^{\pm}$. Figure 1 illustrates the homoclinic explosion on the level of the rearrangement of the one-dimensional manifolds involved; note that this type of representation is

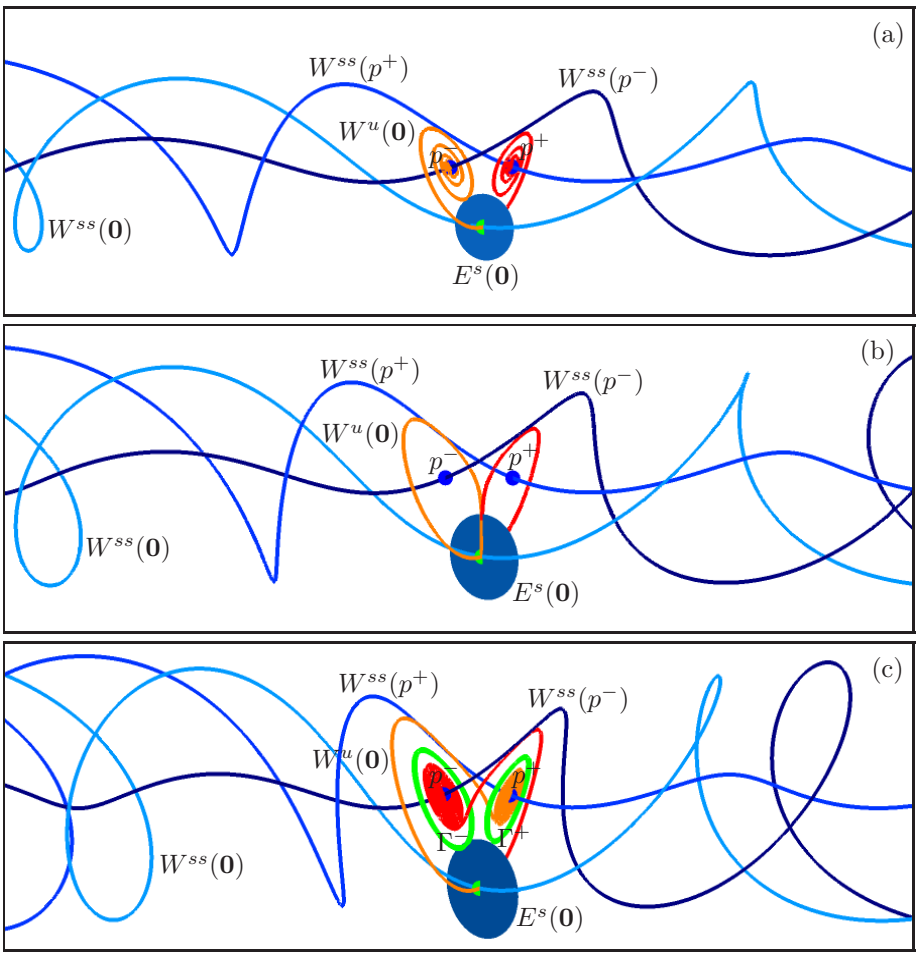

Figure 1: Transition through the homoclinic bifurcation at $\varrho = \varrho_{\text{hom}} \approx 13.9265$. Shown are the equilibrium $\mathbf{0}$ with its one-dimensional manifolds $W^u(\mathbf{0})$ and $W^{ss}(\mathbf{0})$, and the equilibria $p^\pm$ with their one-dimensional manifolds $W^{ss}(p^\pm)$; the small disk represents the linear stable eigenspace $E^s(\mathbf{0})$. Panel (a) is for $\varrho = 10.0$, panel (b) is at the bifurcation, and panel (c) is for $\varrho = 20$; also shown in (c) are the bifurcating periodic orbits $\Gamma^\pm$.

what one typically finds in the literature. Before the bifurcation, in panel (a), the right branch of the unstable manifold $W^u(\mathbf{0})$ (which starts near $\mathbf{0}$ with positive values of x) tends to the right equilibrium p^+ in a spiralling fashion and, similarly, the left branch of $W^u(\mathbf{0})$ spirals into p^-. Notice that, locally near the origin $\mathbf{0}$, the linear stable eigenspace $E^s(\mathbf{0})$ is an approximation of the separatrix $W^s(\mathbf{0})$ between the two basins $\mathcal{B}(p^\pm)$ of $p^\pm$. At the global

bifurcation, when $\varrho = \varrho_{\text{hom}}$, one finds a symmetric pair of homoclinic orbits, meaning that $W^u(\mathbf{0})$ returns to $\mathbf{0}$ tangent to the positive z-axis (which is a subset of $E^s(\mathbf{0})$); see Fig. 1(b). For $\varrho > \varrho_{\text{hom}}$ as in panel (c), a symmetric pair of primary saddle periodic orbits $\Gamma^{\pm}$ bifurcates from the homoclinic orbit. Notice further that both branches of $W^u(\mathbf{0})$ still spiral into p^+ and p^-, but now the right branch spirals into p^- and the left branch spirals into p^+. As before the bifurcation, $E^s(\mathbf{0})$ is an approximation of the local separatrix $W^s(\mathbf{0})$ between the two basins. For each case in Fig. 1 we also included the one-dimensional strong stable manifolds $W^{ss}(\mathbf{0})$ and $W^{ss}(p^{\pm})$ to give an initial idea of the global behaviour; since these curves are not changing qualitatively, one gets the impression that the overall dynamics is not affected much by the homoclinic bifurcation.

1.1. Homoclinic explosion and preturbulent regime

Needless to say, Fig. 1 is rather deceiving. The homoclinic bifurcation does not just give rise to a symmetric pair of primary saddle periodic orbits $\Gamma^{\pm}$. More importantly, for $\varrho > \varrho_{\text{hom}}$ one finds many more saddle periodic and homoclinic orbits in a tubular neighbourhood of the pair of homoclinic orbits. Because it generates all chaotic dynamics in the Lorenz system in this way, the homoclinic bifurcation at $\varrho = \varrho_{\text{hom}}$ is also referred to as a homoclinic explosion point [42]. This statement can be made precise via the description of the Lorenz system by the one-dimensional discontinuous Lorenz map [1, 14, 39, 45]. The Lorenz map describes the dynamics of leaves of the strong stable foliation of the local Poincaré return map to the section $\Sigma_\varrho = \{z = \varrho - 1\}$ through the two secondary equilibria. The planar section Σ_ϱ is the standard choice in the literature [13, 42], because it intersects the attractors of the system (including the Lorenz attractor for $\varrho = 28$); hence, the local return map to Σ_ϱ gives information about the dynamics and bifurcations on the attractors.

It is an important observation that the chaotic dynamics (including all bifurcating periodic orbits) that are created at the homoclinic explosion point at $\varrho = \varrho_{\text{hom}}$ are initially of saddle type [12, 42]. In other words, the secondary equilibria $p^{\pm}$ remain the only attractors, and the question arises whether there is any discernible change at all to the observed dynamics of the Lorenz system after the homoclinic bifurcation. This question has been addressed by Kaplan and Yorke in [24], who found trajectories that make an arbitrarily large number of switches between rotations around p^+ and p^-, respectively, before eventually converging to one of these two point attractors. Kaplan

and Yorke introduced the term preturbulence for this dynamical regime of the Lorenz system — a precursor to the notion of turbulence as introduced in the famous paper [40] by Ruelle and Takens — and they were able to explain it by the existence of a hyperbolic basic set, also refered to as a chaotic saddle. Specifically, Kaplan and Yorke showed in [24] that there exists a Smale horseshoe in the Poincaré map. The chaotic saddle is its suspension and it follows, in particular, that there are infinitely many periodic orbits of saddle type; see also [13, 21]. Statistical properties of this transient chaos in the preturbulent regime were considered in [46] via a numerical study of the one-dimensional Lorenz map. Kaplan and Yorke found that they "seem to observe this entire structure [of a chaotic saddle] persisting and growing until r [ϱ in our notation] reaches the next critical value, $r_1 \approx 24.06$" [24, p. 107]. At this value, $\varrho = \varrho_{\rm het} \approx 24.0579$, the preturbulent regime ends and a chaotic attractor is created at a codimension-one heteroclinic bifurcation, where one finds a symmetric pair of heteroclinic connections from $\mathbf{0}$ to $\Gamma^{\pm}$; for $\varrho > \varrho_{\rm het}$ the unstable manifold $W^u(\mathbf{0})$ cannot 'reach' $p^{\pm}$ any longer and instead accumulates on a chaotic attractor. The chaotic attractor initially coexists with the stable equilibria until $p^{\pm}$ become saddles in the subcritical Hopf bifurcation at $\varrho = \varrho_H$. For further details on the sequence of global bifurcations that one encounters for increasing ϱ see [10] and references therein.

1.2. The role of global manifolds

The question we concentrate on in this paper is how the overall organisation of the entire three-dimensional phase space of the Lorenz system (1) changes in the transition through the homoclinic explosion point at $\varrho = \varrho_{\rm hom}$. More specifically, we consider the topological properties of relevant two-dimensional global invariant manifolds before and after the homoclinic bifurcation at $\varrho = \varrho_{\rm hom}$. A central object of study is the two-dimensional Lorenz manifold $W^s(\mathbf{0})$, which is (at least locally near $\mathbf{0}$) a separatrix between the basins of attraction of the two stable equilibria $p^{\pm}$. The global structure of this manifold as a basin boundary between the two attracting equilibria has actually been studied already by Jackson in the 1980s in two papers [22, 23], which appear to have escaped the attention of the dynamical systems community. (We only discovered these papers during the writing-up of this paper, and quite by accident.) In [22] Jackson is concerned with the case where $1 \leq \varrho \leq \varrho_{\rm hom}$. He considers several sections in phase space and determines — by means of numerical simulation — whether points end up

at p^+ and p^-; the position of the respective intersection of $W^s(\mathbf{0})$ with the section is then deduced as the boundary between the two sets. In this way, Jackson produced sketches of $W^s(\mathbf{0})$ as a two-dimensional surface in $\mathbb{R}^3$; in particular, his sketches show how $W^s(\mathbf{0})$ is able to spiral around the one-dimensional strong stable manifolds $W^{ss}(p^\pm)$, while simultaneously forming a helix locally near the positive z-axis.

Jackson's second paper [23] deals with the structure of $W^s(\mathbf{0})$ for $\varrho_{\text{hom}} \leq \varrho \leq \varrho_{\text{het}}$. He presents a sketch of $W^s(\mathbf{0})$ at $\varrho = \varrho_{\text{hom}}$, showing clearly how it returns to itself along the strong stable manifold $W^{ss}(\mathbf{0})$; compare with the sketch by Perelló in [38] (reproduced in [10]). Jackson observes that it follows from Kaplan and Yorke's work in [24] that the saddle periodic orbits, which are part of the chaotic saddle, and their stable manifolds must lie in the α-limit set of $W^s(\mathbf{0})$. He speaks of $W^s(\mathbf{0})$ as "convoluted" for this reason, and presents a number of sketches of how this two-dimensional manifold returns to a vicinity of the origin. In particular, he determines, by means of careful numerical simulations, the symbolic dynamics (of a shift on two symbols) of the intersection points of $W^s(\mathbf{0})$ with the diagonal $x = y$ in the standard Poincaré section $\Sigma_\varrho = \{z = \varrho - 1\}$. Jackson observes that the boundary between the two basins also contains the stable manifolds of saddle periodic orbits, but does not attempt to find them; rather, he states: "No way has yet been found to represent this highly convoluted set of surfaces" [23, p. 32].

In this paper we show how the Lorenz manifold $W^s(\mathbf{0})$, as well as the stable manifolds $W^s(\Gamma^\pm)$ of the main bifurcating saddle periodic orbits Γ^+ and Γ^-, organise the overall phase space of the Lorenz system before and after the homoclinic bifurcation at $\varrho = \varrho_{\text{hom}}$. To this end, we do not consider intersections of these manifolds with planar sections, but rather their intersection curves with a sufficiently large sphere, denoted S_R, that encloses the attracting equilibria $p^\pm$ as well as the entire one-dimensional unstable manifold $W^u(\mathbf{0})$. The advantage is that the sphere S_R is compact, which allows us to study in a convenient way how the basins of attraction $\mathcal{B}(p^\pm)$ of $p^\pm$ change at $\varrho = \varrho_{\text{hom}}$; in particular, the locations in phase space where long transients occur due to the intermingling of the two basins are determined in this way. Moreover, we are able to give a topological characterisation of the sets of intersection curves of the two-dimensional manifolds $W^u(\mathbf{0})$ and $W^s(\Gamma^\pm)$ with the sphere S_R.

Our study of the overall structure of the dynamics of the Lorenz system in the preturbulent regime is made possible by the recent development of advanced numerical methods for the accurate computation of two-

dimensional global invariant manifolds and their intersection curves with selected codimension-one submanifolds (such as the sphere S_R). Indeed, it is no longer necessary to deduce the position of the Lorenz manifold $W^s(\mathbf{0})$ only indirectly from the knowledge of the basins. Furthermore, the stable manifolds $W^s(\Gamma^{\pm})$ can be computed directly as well. The key idea behind these computations is to continue a suitable family of orbit segments as solutions of well-posed two-point boundary value problems, for example, with the package AUTO [9]. We briefly discuss the numerical methods we use in Appendix A and refer to [26, 27, 28] for further details.

1.3. Numerical evidence versus computer-assisted proofs

From the very beginning, researchers have used numerical investigations to make important contributions to the understanding of the Lorenz system. Not only were new phenomena discovered in this way, but numerical evidence also informed the development of the geometrical theory of the Lorenz system. Initially and traditionally, numerical simulation, that is, the solution of the initial value problem by numerical integration, has been the method of choice. Already Lorenz [29] used numerical simulation not only to demonstrate sensitive dependence on the initial condition, but also to study the geometric organisation of phase space and to derive a return map by plotting successive 'relative maxima' against each other. The homoclinic explosion, and the horseshoe dynamics in the preturbulent regime after the homoclinic explosion, were found by Kaplan and Yorke [24, 46] by careful numerical simulation. The same applies to the many other dynamic features that were reported in the well-known book by Sparrow [42]. Similarly, the organization of phase space by the stable manifold of the origin was initially investigated only indirectly by considering the results of numerical integrations from suitably chosen initial conditions; see [22, 23, 38]. Numerical evidence also formed the basis for the formulation of the observed dynamics in terms of the abstract geometric Lorenz attractor [14, 45], which is assumed to satisfy certain geometric hypotheses. Overall, the rationale has been to develop theory that is consistent with the available numerical evidence. The work presented here is in the same spirit. More specifically, we provide numerical evidence for a consistent picture of how the phase space of the Lorenz system is organized in the preturbulent regime. To this end, we make use of recent and accurate numerical techniques that are based on solving families of appropriately defined boundary value problems.

In spite of its proven use for gaining insights into the dynamics, numerical evidence does not constitute a mathematical proof of a given property of the Lorenz system. Similarly, the fact that chaos and other dynamics has been proven to exist in the geometric Lorenz model does not constitute a proof that they exist in the Lorenz system itself. This gap between numerical evidence and a mathematical statement may be overcome by computer-assisted proofs, which allow one to check that theory and numerical observation indeed agree. The underlying idea is to augment standard numerical computations with rigorous estimates for the computational errors via interval-arithmetic techniques to ensure that certain (topological or geometrical) properties are satified.

We now discuss briefly what has been achieved with rigorous numerical methods for the Lorenz system, where the emphasis has been on showing that there is indeed chaotic dynamics. Best known is the celebrated result by Tucker [43] that the Lorenz system is chaotic for the classical parameter values $\sigma = 10$, $\beta = 8/3$ and $\varrho = 28$. More specifically, Tucker showed that in a small neighborhood of this parameter point the technical conditions of the abstract geometric Lorenz attractor are satisfied. Hence, the Lorenz system itself has a chaotic attractor for the classical parameter values. This computer-assisted proof requires a careful consideration of how trajectories pass near the origin; see also the review by Viana [44]. A different and earlier approach to showing that the Lorenz system has chaotic dynamics (albeit not necessarily of an attracting nature) is to consider specific dynamical objects. The existence of the homoclinic orbit at the first homoclinic explosion point was proved by a rigorous shooting method by Hassard and Zhang [17], thus completing an outline of proof by Hasting and Troy [19]. These authors extended their method in [18] to provide a computer-assisted proof that there are chaotic dynamics in the Lorenz system, namely for $\sigma = 10$, $\beta = 9$ and $\varrho = 76$. The existence of further homoclinic orbits in certain ranges of parameters was established with rigorous computations by Chen [4, 5]. Indeed, the existence of a (symmetric pair of) homoclinic orbits implies the existence of shift dynamics in the Poincaré return map (see, for example, [20, 21]), but it is also possible to verify this directly. Chen showed in [6] that there exists full shift dynamics on two symbols for certain parameter values where ϱ is large. The first computer-assisted proof of the existence of chaotic dynamics for the classical parameter values $\sigma = 10$, $\beta = 8/3$ and $\varrho = 28$ is due to Galias and Zgliczynski [11], who showed the existence of a topological horseshoe in the second iterate of its Poincaré map on the

standard section Σ_ϱ. Using the more elaborate topological tool of Conley index theory, Mischaikow and Mrozek [33, 34] showed the existence of specific subshift dynamics and, hence, positive topological entropy in the Lorenz system, initially for $\sigma = 45$, $\beta = 10$ and $\varrho = 54$, and later with Szymczak [35] also for the classic parameter values.

While rigorous computational techniques can be used to prove properties of the Lorenz system, such computer-assisted proofs are still very subtle and demanding. This is a consequence of the sensitivity of the system with extreme expansion near stable manifolds due to close passages near the origin. Most computer assisted proofs hold only in small neighborhoods of chosen individual parameter points, and the challenge is to provide rigorous statements over larger parameter ranges. A result in this direction is the recent work by Makino *et al.* [31], who used a Taylor model-based integrator [30] to prove the existence of a topological horseshoe in the second iterate of the Poincaré map for $\sigma = 45$, $\beta = 10$ and $\varrho \in [25, 95]$.

To return to the subject of preturbulence of this paper, the proof of existence in [17] of the homoclinic orbit at ϱ_{hom} implies as a corollary that a chaotic saddle exists for $\varrho > \varrho_{\mathrm{hom}}$ sufficiently close to ϱ_{hom}. Moreover, it seems that the method of proof in [31] may be extended to cover (at least some of) the remaining gap of ϱ-values up to $\varrho = 25$. In summary, the existence of horseshoe dynamics and the associated chaotic saddle for $\varrho_{\mathrm{hom}} \leq \varrho \leq \varrho_{\mathrm{het}}$ as reported in Secs. 1.1 and 1.2 is confirmed by all available numerical evidence. This evidence includes the results presented here, which we hope will stimulate further developments in both theory and rigorous computation.

The paper is organised as follows. In the next section we give a brief overview of the invariant objects that are important in this study; here, we also specify the sphere S_R and the stereographic projection used to represent the information on it. Section 3 discusses the situation before the homoclinic explosion for the representative case of $\varrho = 10.0$; we use this case also to illustrate how to interpret the role of the invariant manifolds through their intersections with S_R. Section 4 explains how the Lorenz manifold changes during the homoclinic explosion. The characterisation of the basins $\mathcal{B}(p^{\pm})$ and their boundary in the preturbulent regime can be found in Sec. 5. The final Sec. 6 summarises our results and points to future work. A brief discussion of the numerical methods used for the computations is presented in Appendix A.

2. Background and setup

The observations from Fig. 1 are useful, but they are limited to changes of one-dimensional manifolds. In particular, it not clear from the determination of the one-dimensional manifolds how the emergence of a chaotic saddle $\mathcal{S}$ in the homoclinic explosion at $\varrho = \varrho_{\rm hom}$ influences the overall dynamics of the Lorenz system. In fact, to see how and where transient chaos arises in the three-dimensional phase space one needs to consider the associated two-dimensional manifolds and, in particular, the Lorenz manifold $W^s(\mathbf{0})$. An observation that follows from general theory is the following: for $\varrho < \varrho_{\rm hom}$ the stable manifold $W^s(\mathbf{0})$ curves around $W^u(\mathbf{0})$ and extends towards negative values of z; at the homoclinic bifurcation $W^s(\mathbf{0})$ contains $W^u(\mathbf{0})$ and returns back to itself along the strong stable manifold $W^{ss}(\mathbf{0})$; for $\varrho > \varrho_{\rm hom}$, when $W^s(\mathbf{0})$ returns near $\mathbf{0}$ for the first time, $W^u(\mathbf{0})$ curves around it and $W^s(\mathbf{0})$ extends towards positive values of z. However, this local information on how the Lorenz manifold $W^s(\mathbf{0})$ changes when it first returns near the origin still does not explain how the basins $\mathcal{B}(p^+)$ and $\mathcal{B}(p^-)$ change.

What is needed is information on how $W^s(\mathbf{0})$ divides the three-dimensional phase space, and not just near $\mathbf{0}$. To this end, we consider the intersection $\widehat{W}^s(\mathbf{0}) := W^s(\mathbf{0}) \cap S_R$ with a sphere S_R of sufficiently large radius R so that $W^u(\mathbf{0})$ and the attractor(s) it tends to are strictly inside S_R. In other words, irrespective of the exact size of the sphere S_R, the only one-dimensional objects from Fig. 1 that intersect the sphere (in six discrete points) are the strong stable manifolds $W^{ss}(\mathbf{0})$ and $W^{ss}(p^\pm)$; we denote these intersections as $\widehat{W}^{ss}(\mathbf{0}) := W^{ss}(\mathbf{0}) \cap S_R$ and $\widehat{W}^{ss}(p^\pm) := W^{ss}(p^\pm) \cap S_R$, respectively. Generic points on S_R end up at either of the attractors p^+ and p^-, and the goal is to study their two basins $\widehat{\mathcal{B}}(p^+) := \mathcal{B}(p^+) \cap S_R$ and $\widehat{\mathcal{B}}(p^-) := \mathcal{B}(p^-) \cap S_R$.

Studying the Lorenz manifold and associated basins of attraction on a sufficiently large sphere S_R has a number of advantages compared to studying these objects in the Poincaré section usually considered in the literature [13, 42], which is the section $\Sigma_\varrho = \{z = \varrho - 1\}$ through the two secondary equilibria. As mentioned, the sphere S_R is compact so that the intersections of stable manifolds and basins with S_R are bounded sets. Furthermore, these sets do not change qualitatively when the radius R is increased (provided it is large enough as defined above). Hence, in the spirit of bifurcation theory, all information on the global dynamics of the three-dimensional Lorenz system can be represented by a single compact image on the suitably-chosen sphere S_R.

For definiteness, we choose the centre of S_R as the point $(0, 0, \varrho - 1)$, which is the origin of the usual Poincaré section Σ_ϱ; we refer to the circle $S_R \cap \Sigma_\varrho$ as the equator of S_R. Then the north and south poles of S_R are the intersections with the positive and negative z-axis, respectively, which are both points in $\widehat{W}^s(\mathbf{0})$. We define $R = R(\varrho)$ in the following convenient way, which is based on the properties of the strong stable manifolds $W^{ss}(p^\pm)$. Notice from Fig. 1 that the manifolds $W^{ss}(p^\pm)$ do not change qualitatively throughout the homoclinic bifurcation at $\varrho = \varrho_{\rm hom}$; they spiral around the line $\{y = 0; z = \varrho - 1\}$, which is the x-axis in the plane Σ_ϱ. We define the radius $R = R(\varrho)$ such that the sphere S_R goes through the second intersection point of the right branch of $W^{ss}(p^+)$ (the inner spiralling curve in Fig. 1 with the corresponding smallest amplitude of oscillation in z) with Σ_ϱ. This ϱ-dependent choice of R ensures that S_R is sufficiently large for any value of ϱ we consider. Furthermore, it is convenient because in all images the two inner branches of $W^{ss}(p^\pm)$ will be represented by points on the equator of S_R.

The surface of S_R can conveniently be represented by means of stereographic projection; to this end, we project along the positive x-axis by the transformation

$$(x, y, z) \mapsto (u, v) := \left(\frac{y}{x + R}, \frac{z - (\varrho - 1)}{x + R} \right) \tag{3}$$

for $(x, y, z) \in S_R$, that is, satisfying $x^2 + y^2 + (z - \varrho + 1)^2 = R^2$. Due to the symmetry (2) it suffices to show only the half-sphere with $x \geq 0$, which maps onto the unit disk under (3). Hence, we can conveniently represent the entire information on S_R as a single image inside the unit circle; see Sec. 3 for detailed illustrations of this stereographic projection.

3. Global dynamics for $1 < \varrho < \varrho_{\rm hom}$

We first consider the situation for $1 < \varrho < \varrho_{\rm hom} \approx 13.9265$ and show that in this range of ϱ the Lorenz manifold $W^s(\mathbf{0})$ divides the phase space into the two basins $\mathcal{B}(p^+)$ and $\mathcal{B}(p^-)$. In order to get a good feel for the interpretation of the stereographic projection of the information on S_R, we discuss this case in more detail for the representative value $\varrho = 10.0$.

Figure 2 shows an increasingly larger initial piece of $W^s(\mathbf{0})$ for $\varrho = 10.0$ as computed with the geodesic level set growth method from Ref. [26]. Also shown are the equilibria $\mathbf{0}$ and $p^\pm$ and the one-dimensional manifolds $W^u(\mathbf{0})$

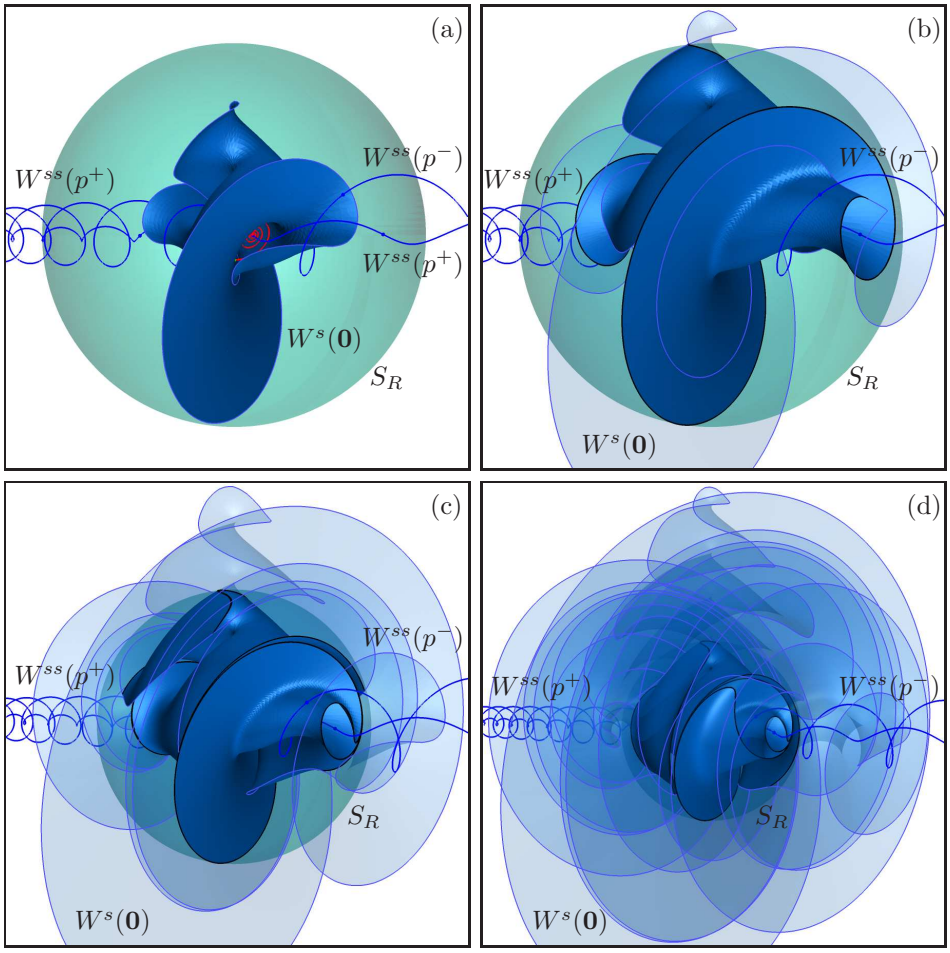

Figure 2: When the Lorenz manifold $W^s(\mathbf{0})$ for $\varrho = 10.0$ is grown in geodesic distance from $\mathbf{0}$ it starts to intersect the sphere S_R with radius $R = 67.1565$; the part of $W^s(\mathbf{0})$ outside S_R is rendered transparent and its outer boundary is the light blue curve. Also shown are the equilibria $\mathbf{0}$ and $p^\pm$ and the one-dimensional manifolds $W^u(\mathbf{0})$ and $W^{ss}(p^\pm)$; compare with Fig. 1(a). From (a) to (d), $W^s(\mathbf{0})$ has been computed up to geodesic distances 58.0, 91.0, 129.0 and 193.0.

and $W^{ss}(p^\pm)$; compare with Fig. 1(a). In Fig. 2(a) the computed piece of the Lorenz manifold $W^s(\mathbf{0})$ is still strictly inside the sphere S_R (whose radius $R = 67.1565$ is determined by the condition on $W^{ss}(p^\pm)$ introduced in the previous section). As $W^s(\mathbf{0})$ grows, it starts to intersect S_R. In Fig. 2(b)–(d) the respective part of $W^s(\mathbf{0})$ inside S_R is rendered as a solid surface, while

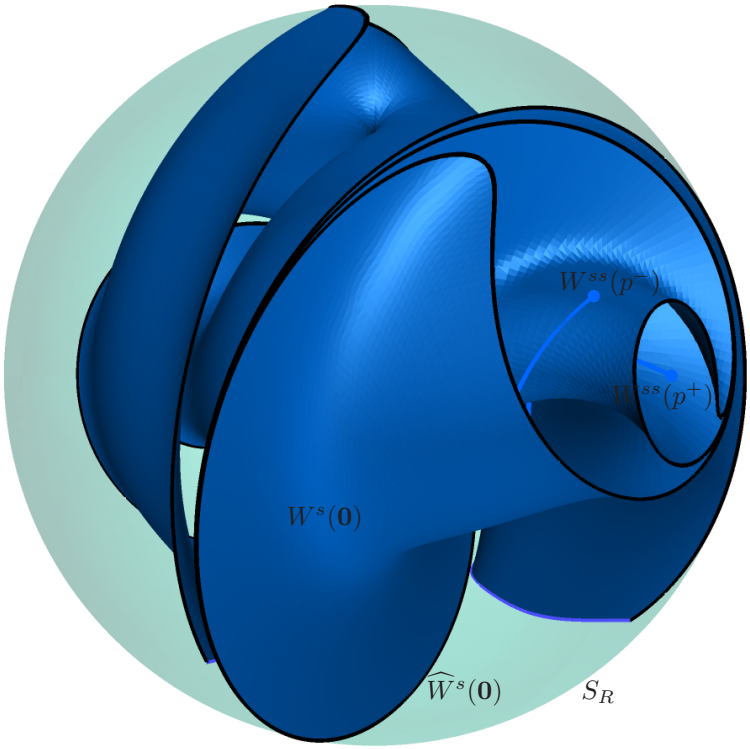

Figure 3: The part of the Lorenz manifold $W^s(\mathbf{0})$ for $\varrho = 10.0$ that lies inside the sphere S_R with radius $R = 67.1565$; here $W^s(\mathbf{0})$ has been computed up to geodesic distance 193.0 as in Fig. 2(d).

the part of $W^s(\mathbf{0})$ outside S_R is rendered as a transparent surface. The outer geodesic level set (which is a smooth, unknotted closed curve) is highlighted. Figure 2 illustrates the intriguing geometry of the Lorenz manifold $W^s(\mathbf{0})$, which is quite surprising in light of the fact that the computed part of it is topologically simply a disk. Notice, in particular, from Fig. 2(d) how $W^s(\mathbf{0})$ scrolls around the one-dimensional strong stable manifolds $W^{ss}(p^{\pm})$ in a complicated way.

Figure 3 shows the part of $W^s(\mathbf{0})$ for $\varrho = 10.0$, computed up to geodesic distance 193.0, that lies inside the sphere S_R. The intersection $\widehat{W}^s(\mathbf{0})$ is highlighted as a black curve. Notice again how $W^s(\mathbf{0})$ scrolls around $W^{ss}(p^+)$ and $W^{ss}(p^-)$. The idea is now to consider only the set $\widehat{W}^s(\mathbf{0})$ on the surface of S_R (together with the points $\widehat{W}^{ss}(p^+)$ and $\widehat{W}^{ss}(\mathbf{0})$). Figure 3 has been

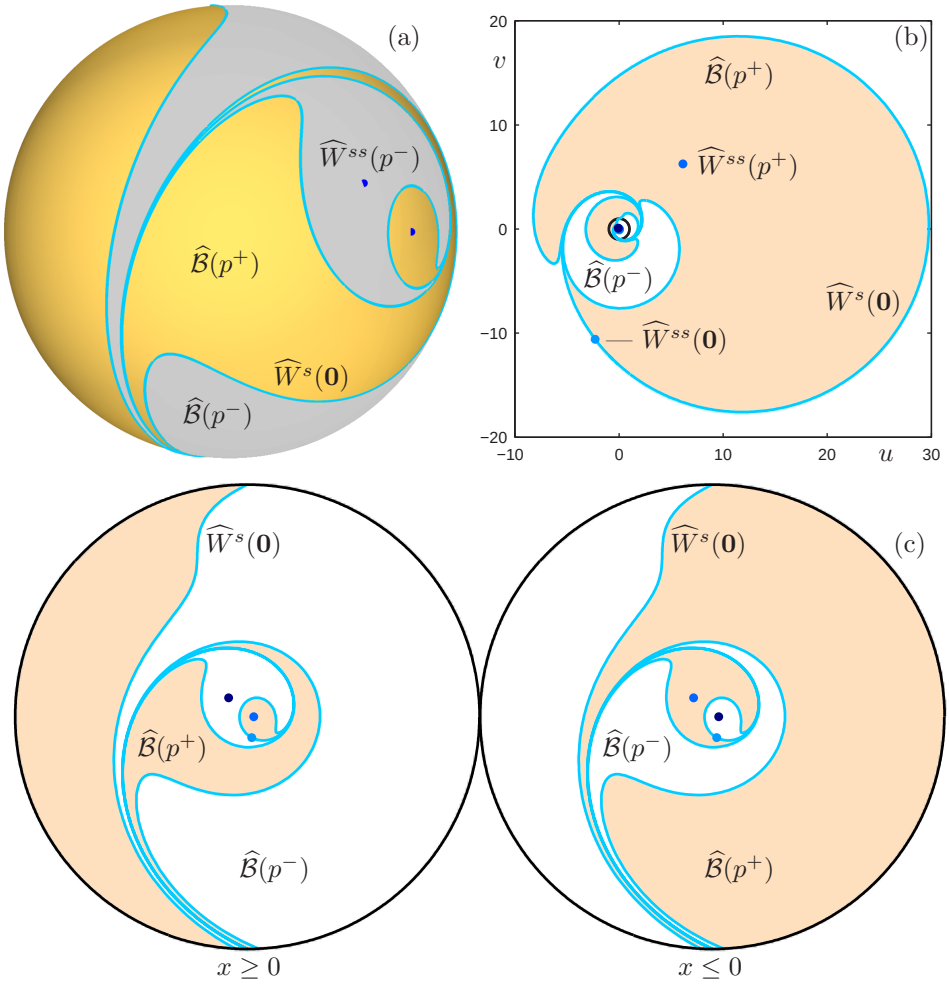

Figure 4: The intersection curve $\widehat{W}^s(\mathbf{0})$ and the points $\widehat{W}^{ss}(\mathbf{0})$ and $\widehat{W}^{ss}(p^{\pm})$ for $\varrho = 10.0$, shown on the sphere S_R for $R = 67.1565$ (a) and in stereographic projection (b). Panel (c) shows the stereographic projections inside the unit circle of the two symmetrically-related halves of S_R for $x \geq 0$ and for $x \leq 0$; the basin of attraction $\widehat{\mathcal{B}}(p^+)$ is shaded.

obtained by clipping off the part of $W^s(\mathbf{0})$ that lies outside S_R, which also reveals its intersection with S_R. However, if one is interested chiefly in the set $\widehat{W}^s(\mathbf{0})$ then it is numerically advantageous to compute it with a boundary value setup directly as (a set of) one-dimensional curves [2, 27]; see Appendix A for more information on how this can be achieved.

Figure 4(a) shows the set $\widehat{W}^s(\mathbf{0})$ for $\varrho = 10.0$ on the sphere S_R. It is not

immediately obvious from this image, but $\widehat{W}^s(\mathbf{0})$ is actually a single simple closed curve on S_R that passes very close to itself in the region of negative z; compare also with Fig. 3 (where the curve is not yet closed because the computed part of $W^s(\mathbf{0})$ is still not quite large enough). The closed curve $\widehat{W}^s(\mathbf{0})$ has finite arclength and divides S_R into the two basins $\widehat{\mathcal{B}}(p^+)$ and $\widehat{\mathcal{B}}(p^-)$, which are topological disks. The basins can be identified from the fact that $\widehat{W}^{ss}(p^+)$ lies in $\widehat{\mathcal{B}}(p^+)$ and $\widehat{W}^{ss}(p^-)$ lies in $\widehat{\mathcal{B}}(p^-)$.

Figure 4(b) shows the stereographic projection of S_R by (3) onto the (y, z)-plane along the direction of decreasing x. This representation allows one to check the properties above, but it is not very convenient due to considerable distortion. To deal with this issue, we present in Fig. 4(c) the stereographic projections onto the unit disk of the two hemispheres of S_R for $x \geq 0$ and for $x \leq 0$. Notice that the two projections can be stitched together along the unit circle to recreate the entire information on the sphere S_R. What is more, due to the symmetry (2) of the Lorenz system, the hemisphere for $x \leq 0$ is identical to that for $x \geq 0$ modulo an exchange of the basins $\widehat{\mathcal{B}}(p^+)$ and $\widehat{\mathcal{B}}(p^-)$. In other words, we can represent the dynamics of the Lorenz system in the wider phase space by a single, planar image of the organisation of manifolds and basins inside the unit disk. From now on, we illustrate the overall dynamics of the Lorenz system (1) by showing only the part of the stereographic projection of the intersections of the manifolds with S_R that corresponds to the hemisphere $x \geq 0$, that is, the left unit disk in Fig. 4(c).

Let us briefly discuss in more detail the influence of the radius R of the chosen sphere S_R. When R is increased, the set $\widehat{W}^s(\mathbf{0})$ remains a simple closed curve, but it winds more and more around the points $\widehat{W}^{ss}(p^+)$ and $\widehat{W}^{ss}(p^-)$. This is a result of the helical nature of the one-dimensional manifolds $W^{ss}(p^\pm)$; compare with Fig. 1(a). Importantly, however, the topological nature of the basins $\widehat{\mathcal{B}}(p^\pm)$ and their boundary $\widehat{W}^s(\mathbf{0})$ does not change qualitatively in the process. This means that the information on S_R for sufficiently large R indeed represents the overall dynamics of the Lorenz system in its three-dimensional phase space. This statement is correct throughout the range of ϱ. For the particular case of $1 < \varrho < \varrho_{\text{hom}}$ we can indeed see how the two-dimensional Lorenz manifold $W^s(\mathbf{0})$ divides $\mathbb{R}^3$ into the two basins $\mathcal{B}(p^+)$ and $\mathcal{B}(p^-)$, which are each other's images under the symmetry transformation (2).

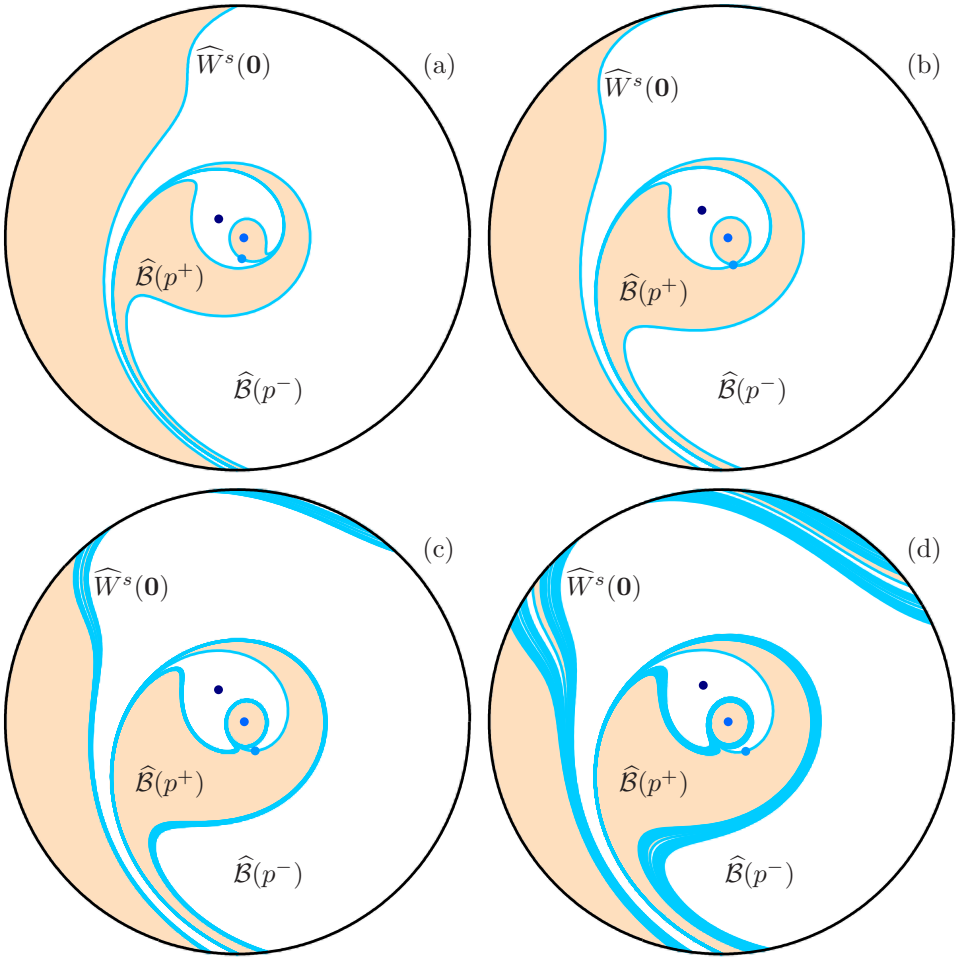

Figure 5: Stereographic projection of sphere S_R for $x \geq 0$, showing $\widehat{W}^s(\mathbf{0})$, $\widehat{W}^{ss}(\mathbf{0})$, $\widehat{W}^{ss}(p^\pm)$ and $\widehat{\mathcal{B}}(p^\pm)$ for $\varrho = 10.0$ (a), $\varrho = 13.9 \approx \varrho_{\rm hom}$ (b), $\varrho = 16.0$ (c), and $\varrho = 18.0$ (d); the basin $\widehat{\mathcal{B}}(p^+)$ is shaded.

4. Bifurcation of $W^s(0)$ at $\varrho = \varrho_{\rm hom}$

Figure 5 shows how the Lorenz manifold $\widehat{W}^s(\mathbf{0})$ on the sphere S_R changes when the parameter ϱ is increased through $\varrho_{\rm hom}$. Panel (a) shows the situation for $\varrho = 10.0$, which is representative for $1 < \varrho < \varrho_{\rm hom}$; as we discussed, the set $\widehat{W}^s(\mathbf{0})$ is a simple closed curve of finite arclength. At the moment of homoclinic bifurcation at $\varrho = \varrho_{\rm hom}$, which is illustrated in Fig. 5(b) for the

sufficiently close value of $\varrho = 13.9$, the stable manifold $W^s(\mathbf{0})$ returns back to itself exactly at the strong stable manifold $W^{ss}(\mathbf{0})$. As a result, $\widehat{W}^s(\mathbf{0})$ still has finite arclength but is no longer a simple closed curve; it can be thought of as a closed curve with two points of transverse self-intersection, at the two points $\widehat{W}^{ss}(\mathbf{0}) \approx (\pm 66.0041, \pm 6.9372, -2.7554)$. As a consequence, the two basins $\widehat{\mathcal{B}}(p^+)$ and $\widehat{\mathcal{B}}(p^-)$ on S_R now each consist of two disjoint regions, which are both topological disks.

Figures 5(c) and (d) show the stereographic projections of $\widehat{W}^s(\mathbf{0})$ for $\varrho_{\rm hom} < \varrho < \varrho_{\rm het}$, namely, for $\varrho = 16.0$ and $\varrho = 18.0$, respectively. The set $\widehat{W}^s(\mathbf{0})$ is no longer a simple closed curve of finite arclength. Rather, this set consists of infinitely many curves that form well-defined bands on S_R that increase in width as ϱ increases; compare panels (c) and (d). The major regions of the two basins $\widehat{\mathcal{B}}(p^+)$ and $\widehat{\mathcal{B}}(p^-)$ have been identified, but it is now not immediately clear how the many smaller regions should be shaded. Our computations show that each path-connected component of the set $\widehat{W}^s(\mathbf{0})$ is actually a curve of infinite arclength whose two ends each accumulate on a topological circle (a simple closed curve); note that in this accumulation process the integration time needed for the computation of the corresponding orbit segments goes to infinity. One of these topological circles bounds the region of $\widehat{\mathcal{B}}(p^+)$ that contains $\widehat{W}^{ss}(p^+)$ in the centre of Figs. 5(c) and (d); the other bounds the region of $\widehat{\mathcal{B}}(p^-)$ that contains $\widehat{W}^{ss}(p^-)$ (which is on the other side of the sphere S_R that is not shown in panels (c) and (d)). In particular, it follows that for $\varrho_{\rm hom} \leq \varrho < \varrho_{\rm het}$ the basins $\widehat{\mathcal{B}}(p^\pm)$ are no longer connected.

In spite of its complicated structure, the set $\widehat{W}^s(\mathbf{0})$ locally separates $\mathcal{B}(p^+)$ and $\mathcal{B}(p^-)$. This means that for every point $w \in \widehat{W}^s(\mathbf{0})$ there is a neighbourhood $N(w) \subset S_R$ such that $\widehat{W}^s(\mathbf{0}) \cap N(w)$ is a single curve of finite arclength that divides $N(w)$ into two sets $\widehat{\mathcal{B}}(p^+) \cap N(w)$ and $\widehat{\mathcal{B}}(p^-) \cap N(w)$ that are topological disks; the single arc of $\widehat{W}^s(\mathbf{0})$ in the centre of Figs. 5(c) and (d) clearly illustrates this property. In particular, it follows that $\widehat{W}^s(\mathbf{0})$ is locally connected and accessible from both sides, that is, both from $\widehat{\mathcal{B}}(p^+)$ and from $\widehat{\mathcal{B}}(p^-)$. In turn, also the two-dimensional Lorenz manifold $W^s(\mathbf{0}) \subset \mathbb{R}^3$ is locally connected, locally separates $\mathcal{B}(p^+)$ and $\mathcal{B}(p^-)$ and is accessible from both sides.

5. Characterisation of preturbulence in phase space

It is an important realisation that for $\varrho_{\rm hom} < \varrho < \varrho_{\rm het}$ the boundary of the two basins $\mathcal{B}(p^{\pm})$ is no longer formed by $W^s(\mathbf{0})$ alone. This follows from the fact that close to the attractors p^+ and p^- the basin is formed by the stable manifolds $W^s(\Gamma^+)$ and $W^s(\Gamma^-)$ of the two bifurcating saddle periodic orbits Γ^+ and Γ^-. Locally near Γ^+ and Γ^- these two-dimensional manifolds are topological cylinders that surround the points p^+ and p^- and their strong stable manifolds $W^{ss}(p^+)$ and $W^{ss}(p^-)$, respectively. Furthermore, the manifold $W^s(\Gamma^+)$ surrounds the left branch of the one-dimensional unstable manifold $W^u(\mathbf{0})$ (which spirals to p^+); compare with Fig. 1(c). This implies that near the origin $\mathbf{0}$ the basin $\mathcal{B}(p^+)$ is bounded by both $W^s(\Gamma^+)$ and $W^s(\mathbf{0})$, and similarly for $\mathcal{B}(p^-)$. Hence, in order to understand what happens to $\mathcal{B}(p^{\pm})$ as ϱ passes through $\varrho_{\rm hom}$, we must consider not only $W^s(\mathbf{0})$ but also $W^s(\Gamma^{\pm})$.

Figure 6 shows the situation on S_R for $\varrho = 18.0$. Panel (a) shows $\widehat{W}^s(\Gamma^+) := W^s(\Gamma^+) \cap S_R$, and panel (b) shows $\widehat{W}^s(\Gamma^-) := W^s(\Gamma^-) \cap S_R$. The positive side of the two-dimensional manifold $W^s(\Gamma^+)$ intersects S_R in a topological circle that bounds the central component of $\widehat{\mathcal{B}}(p^+)$ that contains $W^{ss}(p^+)$; similarly, the negative side of $W^s(\Gamma^-)$ intersects S_R in a topological circle that bounds the central component of $\widehat{\mathcal{B}}(p^-)$ that contains $W^{ss}(p^-)$. Note that $\widehat{W}^s(\mathbf{0})$ accumulates exactly on these two circles; compare with Figs. 5 (c) and (d). The negative side of $W^s(\Gamma^+)$ intersects S_R in a set that contains infinitely many curves of infinite arclength. The two ends of each such curve also accumulate on the two topological circles in $W^s(\Gamma^+)$ and $W^s(\Gamma^-)$, respectively. Due to symmetry, the same statement holds for $W^s(\Gamma^-)$. Furthermore, the curves in $W^s(\Gamma^{\pm})$ can be found in the same bands on S_R as those in $\widehat{W}^s(\mathbf{0})$. In the stereographic view of the half-sphere for $x \geq 0$, the two images of $\widehat{W}^s(\Gamma^+)$ and $\widehat{W}^s(\Gamma^-)$ in Fig. 6(a) and (b) appear to be identical, but this is not the case. Rather, due to symmetry, $\widehat{W}^s(\Gamma^-)$ in panel (b) is identical to $\widehat{W}^s(\Gamma^+)$ on the half-sphere for $x \leq 0$, and vice versa. Indeed, the sets of curves in Figs. 6(a) and (b) connect at the bounding unit circle.

Figure 6(c) shows all three manifolds, $\widehat{W}^s(\mathbf{0})$, $\widehat{W}^s(\Gamma^+)$ and $\widehat{W}^s(\Gamma^-)$ on the half-sphere for $x \geq 0$. In this view, it is clear that the three different manifolds are very close to one another. Figure 6(d) is an enlargement that emphasises the structure of the three sets of curves and the two basins $\widehat{\mathcal{B}}(p^+)$ and $\widehat{\mathcal{B}}(p^-)$.

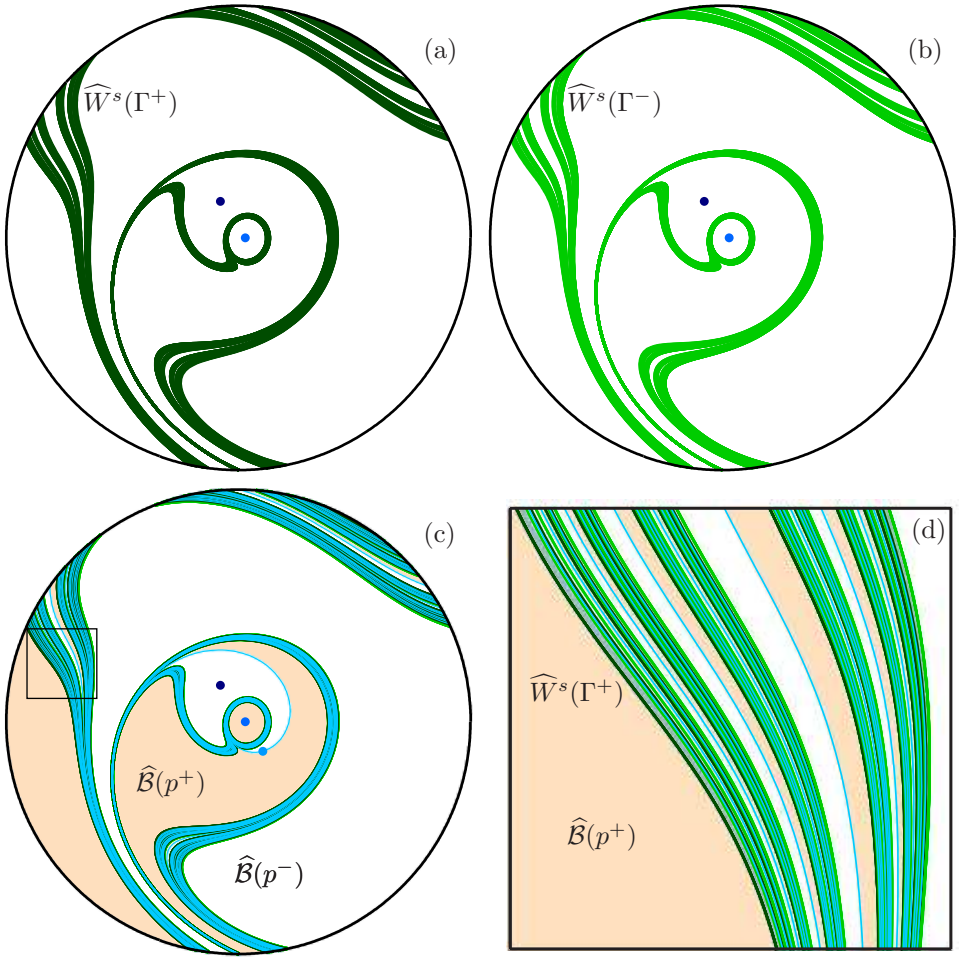

Figure 6: Stereographic projection of the sphere S_R for $x \geq 0$ for $\varrho = 18.0$. Panel (a) shows $\widehat{W}^s(\Gamma^+)$, panel (b) shows $\widehat{W}^s(\Gamma^-)$, panel (c) shows all three sets $\widehat{W}^s(\mathbf{0})$, $\widehat{W}^s(\Gamma^+)$ and $\widehat{W}^s(\Gamma^-)$, and panel (d) is an enlargement inside the box $[-0.91, -0.61] \times [0.1, 0.4]$. Also shown are $\widehat{W}^{ss}(\mathbf{0})$ and $\widehat{W}^{ss}(p^\pm)$; the basin $\widehat{\mathcal{B}}(p^+)$ is shaded.

This image clearly reveals a Cantor structure. Bi-coloured strips are visible that each are divided by a single and isolated curve of $\widehat{W}^s(\mathbf{0})$ into two sub-strips, one belonging to $\widehat{\mathcal{B}}(p^+)$ and the other belonging to $\widehat{\mathcal{B}}(p^-)$, respectively; this illustrates the locally separating nature of $\widehat{W}^s(\mathbf{0})$ at increasingly smaller scale. Each bicoloured strip is bounded by a curve in $\widehat{W}^s(\Gamma^+)$ on the left and

by a curve in $\widehat{W}^s(\Gamma^-)$ on the right, which in turn are the limits on one side of three sets of accumulating curves in $\widehat{W}^s(\mathbf{0})$ and $\widehat{W}^s(\Gamma^\pm)$.

The Cantor structure in Fig. 6 illustrates the manifestation of preturbulence in phase space. Large regions of the basins $\widehat{\mathcal{B}}(p^+)$ and $\widehat{\mathcal{B}}(p^-)$ coexist with arbitrarily thin strips of these basins in certain regions of phase space. An initial condition in any such strip ends up at the respective attractor only after a number of loops around p^+ or p^-. The number of these loops depends on the width of the strip, which reflects 'how deep' the strip is located in the Cantor structure; see also [23]. We remark that this view of the manifestation of preturbulence in the phase space of the Lorenz system is in agreement with the findings in [24, 46]; in particular, it gives a geometric interpretation of the statistical properties found in [46] for the one-dimensional Lorenz map for $\varrho > \varrho_{\rm hom}$.

We now return to the question of the topological nature of the basins $\widehat{\mathcal{B}}(p^\pm)$ and the sets $\widehat{W}^s(\mathbf{0})$ and $\widehat{\mathcal{W}}_{\Gamma^\pm} := \widehat{W}^s(\Gamma^+) \cup \widehat{W}^s(\Gamma^-)$ in their boundary for $\varrho_{\rm hom} < \varrho < \varrho_{\rm het}$. Figure 6 shows that the set $\widehat{\mathcal{W}}_{\Gamma^\pm}$ has a different topology from $\widehat{W}^s(\mathbf{0})$. More specifically, the (local) intersection of $\widehat{\mathcal{W}}_{\Gamma^\pm}$ with any transverse line are the countably many points of a Cantor set that bound the open intervals in its complement; see Fig. 6(d) and the discussion above. This Cantor set is the diffeomorphic image of the corresponding part of the invariant set of the one-dimensional Lorenz map, which is obtained by projecting the return map in the planar section Σ_ϱ along its strong stable manifolds. In particular, it follows that the union $\widehat{\mathcal{W}}_{\Gamma^\pm}$, as well as the two constituent sets $\widehat{W}^s(\Gamma^\pm)$, are locally disconnected. Moreover, the sets $\widehat{W}^s(\Gamma^\pm)$ are accessible only from one side, namely $\widehat{W}^s(\Gamma^+)$ from within the set $\widehat{\mathcal{B}}(p^+)$ and $\widehat{W}^s(\Gamma^-)$ from within the set $\widehat{\mathcal{B}}(p^-)$.

In fact, this is not the whole story. It follows from general theory [24, 23] that $W^s(\mathbf{0})$ accumulates not only on $\mathcal{W}_{\Gamma^\pm}$, but also on the stable manifold $W^s(\mathcal{S})$ of the chaotic saddle $\mathcal{S}$ itself, which contains $\mathcal{W}_{\Gamma^\pm}$ as a dense subset. Indeed, the basins $\widehat{\mathcal{B}}(p^+)$ and $\widehat{\mathcal{B}}(p^-)$ are in the complement of $\widehat{W}^s(\mathcal{S}) = W^s(\mathcal{S}) \cap S_R$, whose intersection with a transverse line is the entire Cantor set. Apart from the primary periodic orbits $\Gamma^\pm$, the chaotic saddle $\mathcal{S}$ contains countably infinitely many additional saddle periodic orbits Γ^k (of higher and higher period), whose two-dimensional stable manifolds $W^s(\Gamma^k)$ intersects S_R in sets $\widehat{W}^s(\Gamma^k) := W^s(\Gamma^k) \cap S_R$ that are not accessible. Each of the sets $\widehat{W}^s(\Gamma^k)$ can be computed, in principle, with the same numerical

technique used to compute $\widehat{W}^s(\Gamma^\pm)$, but this is a considerable computational challenge (especially for larger periods of the periodic orbit) beyond the scope of this paper. The set $\widehat{W}^s(\mathcal{S})$ is closed and bounded and hence, a continuum. More specifically, it is locally a Cantor bundle [15, 16]. We conclude from the properties of the dense subset $\mathcal{W}_{\Gamma^\pm}$ that $\widehat{W}^s(\mathcal{S})$ is an indecomposable continuum on S_R. Indecomposable continua in the plane have been found in a variety of dynamical contexts; see, for example, [7, 41] and the survey paper [25] for further details. In particular, indecomposable continua occur naturally as the closure of stable or unstable manifolds of planar diffeomorphisms such as the Smale horseshoe map, the Hénon map and the Ikeda map.

Overall we conclude from the numerical evidence presented here that the set $\widehat{\mathcal{W}}_{\Gamma^\pm}$, which consists of two topological circles and infinitely many arcs, is the accessible subset of the indecomposable continuum $\widehat{W}^s(\mathcal{S})$. The set $\widehat{W}^s(\mathbf{0})$, on the other hand, is locally connected and accessible globally, and it accumulates on both $\widehat{W}^s(\mathcal{S})$ and its accessible subset $\widehat{\mathcal{W}}_{\Gamma^\pm}$. These properties of their boundary characterise the intricate self-accumulating nature of the two basins $\widehat{\mathcal{B}}(p^+)$ and $\widehat{\mathcal{B}}(p^-)$ on the sphere S_R.

It follows that, when the phase space $\mathbb{R}^3$ is compactified in a suitable fashion (see [32]), the union $\mathcal{W}_{\Gamma^\pm} = W^s(\Gamma^+) \cup W^s(\Gamma^+)$ of the two-dimensional manifolds themselves is the accessible subset of the indecomposable continuum $W^s(\mathcal{S})$. Notice that, in spite of this intriguing property of their boundary, the basins $\mathcal{B}(p^\pm) \subset \mathbb{R}^3$ are simply connected; this is due to the fact that each point in the basin is connected to the attracting point $p^\pm$ by a unique forward trajectory of finite arclength.

6. Conclusions

The transition through the homoclinic explosion point of the Lorenz system results in a dramatic change of the topological structure of the basins of the two attracting equilibria, which remain the only attractors before and after this bifurcation. This was studied here by means of computing the intersection sets of the Lorenz manifold $W^s(\mathbf{0})$ and of the stable manifolds $W^s(\Gamma^\pm)$ of the primary periodic orbits $\Gamma^\pm$ with a sufficiently large sphere. In particular, our computations revealed the bifurcating Cantor structure of invariant manifolds and basins, which explains where in phase space long transients — the characterising feature of preturbulence — can be found. Our study was performed by changing the parameter ϱ of the Lorenz system,

while keeping σ and β fixed at their classical values. However, the change in topology of the associated global invariant manifolds is generic and will, hence, be found for any transverse path in parameter space that crosses the codimension-one surface of this homoclinic bifurcation. We can summarise our findings as follows.

Global invariant manifolds in the transition to preturbulence.

(R1) Regular behaviour for $1 < \varrho < \varrho_{\rm het}$. On any sufficiently large sphere S_R the set $\widehat{W}^s(\mathbf{0}) = W^s(\mathbf{0}) \cap S_R$ is a single closed curve that divides S_R into the two basins $\widehat{\mathcal{B}}(p^+) = \mathcal{B}(p^+) \cap S_R$ and $\widehat{\mathcal{B}}(p^-) = \mathcal{B}(p^-) \cap S_R$, which are topological disks.

(R2) Preturbulence for $\varrho_{\rm hom} < \varrho < \varrho_{\rm het}$. On any sufficiently large sphere S_R the accessible boundary of $\widehat{\mathcal{B}}(p^\pm)$ is formed by $\widehat{W}^s(\mathbf{0})$ and by $\widehat{W}^s(\Gamma^\pm) = W^s(\Gamma^\pm) \cap S_R$. The set $\widehat{W}^s(\mathbf{0})$ is the infinite union of curves of infinite arclength. It accumulates on the union $\widehat{\mathcal{W}}_{\Gamma^\pm} = \widehat{W}^s(\Gamma^+) \cup \widehat{W}^s(\Gamma^-)$, which is the accessible set of an indecomposable continuum, namely the set $\widehat{W}^s(\mathcal{S}) = W^s(\mathcal{S}) \cap S_R$ of a chaotic saddle $\mathcal{S}$. The two basins $\widehat{\mathcal{B}}(p^+)$ and $\widehat{\mathcal{B}}(p^-)$ are intermingled in the sense that they accumulate on $\widehat{\mathcal{W}}_{\Gamma^\pm}$ from one side.

(R3) Limits of preturbulence. The sets $\widehat{\mathcal{W}}_{\Gamma^\pm} \subset \widehat{W}^s(\mathcal{S})$ become geometrically thicker (in Hausdorff dimension [36, 37]) and extends over a larger area on S_R as $\varrho \to \varrho_{\rm het}$. Conversely, for decreasing ϱ, they shrink and eventually converge to $\widehat{W}^s(\mathbf{0})$ for $\varrho = \varrho_{\rm hom}$ in the Hausdorff metric.

These results have been obtained with state-of-the-art efficient and highly accurate numerical computations of two-dimensional invariant manifolds and their intersections with a chosen codimension-one submanifold in phase space. We would argue that these numerical methods, which are based on the continuation of orbit segments defined via suitable two-point boundary problems, have reached a level of maturity that allows for detailed mathematical observations. From a rigorous mathematical perspective, our findings can be viewed as conjectures whose proofs require, first, consideration of which computations are sufficient to establish topological properties of basin boundaries similar to those reviewed in [25] and, second, error estimates for those computations.

Other global bifurcations can be studied in a similar spirit, and the study of the role of two-dimensional global invariant manifolds in such bifurcations is the subject of our ongoing research. First of all, we are studying more global bifurcations in the Lorenz system itself. The transition to chaotic attractors at ϱ_{het}, where one finds a pair of heteroclinic connections from the origin to the primary secondary orbits, will be discussed elsewhere; furthermore, there are (infinitely many) more secondary homoclinic bifurcations in the Lorenz system; see [10, 42]. Secondly, we are considering the role of global invariant manifolds in textbook homoclinic bifurcations of equilibria in three-dimensional vector fields; different cases are distinguished by whether the (stable) eigenvalues are real or complex, and whether the stable manifolds at the moment of homoclinic bifurcation is orientable or not.

Acknowledgements

We dedicate this paper to the memory of Floris Takens. We learnt much of dynamical systems theory from him, and are very grateful for the way he influenced our mathematical thinking.

We thank John Guckenheimer for his helpful comments on a draft of this paper, and the anonomous referees for their constructive criticism. The research of HMO was supported by an EPSRC Advanced Research Fellowship grant, and that of EJD by an NSERC (Canada) Discovery Grant (N00138); furthermore, HMO and BK are grateful for the hospitality of Concordia University during several research visits.

Appendix A. Computation of global invariant manifolds

Stable and unstable manifolds of equilibria and periodic orbits of a given vector field are global objects that need to be found with numerical techniques. One-dimensional stable and unstable manifolds, such as those shown in Fig. 1, can be computed simply by integrating from initial conditions in the respective linear eigenspace and close to the equilibrium. However, higher-dimensional global invariant manifolds, such as the two-dimensional manifolds presented here, cannot be found reliably simply by integration from a set of initial conditions. This is why the development of more advanced numerical methods for the computation of global invariant manifolds has been an active area of research; see, for example, the survey papers [27, 28].

In this paper we make use of two complementary numerical methods: the computation of $W^s(\mathbf{0})$ as a two-dimensional surface with the geodesic level set growth method from Ref. [26], and the computation of one-dimensional curves in the intersection sets $\widehat{W}^s(\mathbf{0})$ and $\widehat{W}^s(\Gamma^{\pm})$ on the sphere S_R [8, 28]. Both methods use the technique of continuation of a suitable family of orbit segments, which are found as solutions of an associated two-point boundary value problem (BVP) with the package AUTO [9].

To compute $W^s(\mathbf{0})$ as a two-dimensional manifold we view it as a one-parameter family of level sets (which are smooth closed curves) of the geodesic distance to the origin. A discrete and uniform mesh is obtained by computing step-by-step a new geodesic level set at a suitable distance from the previous one, according to accuracy criteria that take into account the curvature along geodesics. The first geodesic level set is a circle in the linear stable eigenplane $E^s(\mathbf{0})$ with centre $\mathbf{0}$ and a (small) radius δ; it is represented as a piecewise linear curve through a finite number of equally-spaced mesh points. At each step, the method finds a new point at distance Δ for every point on the previous geodesic level set; this is achieved for each point by solving a BVP that defines orbit segments that start in a plane through the point under consideration and end on the previous geodesic level set. Extra points are added where needed, but in such a way that the total interpolation error is controlled. At the end of each step a new band of the manifold is constructed as a triangulation between the previous and the presently computed geodesic level set; more details and a proof of convergence can be found in [26]. Once the Lorenz manifold $W^s(\mathbf{0})$ has been computed with this method, it can be visualised in different ways as a two-dimensional surface. In particular, a post-processing step allows us to clip off the part of $W^s(\mathbf{0})$ that lies outside S_R, which also reveals the set $\widehat{W}^s(\mathbf{0}) \subset S_R$; see Figs. 2 and 3.

Intersection curves of a two-dimensional global invariant manifold with a chosen codimension-one submanifold in phase space can be computed directly and very accurately with a BVP setup. Here we briefly discuss only how to compute the manifolds under consideration; see [2, 27] for more details of this general approach. Any point in $\widehat{W}^s(\mathbf{0})$ is the begin point of a trajectory that starts on S_R and ends at the origin $\mathbf{0}$. Such a trajectory can be approximated efficiently by an orbit segment (with finite integration time) with begin point on S_R and end point on a small ellipse in $E^s(\mathbf{0})$ around $\mathbf{0}$; as such, it is the solution of a well-posed BVP. Hence, one obtains a one-parameter family of orbit segments by allowing the angular variable of

the ellipse to vary, so that the begin point traces out the sought curve on S_R. The family of orbit segments is computed with the package AUTO [9]. More specifically, AUTO uses pseudo-arclength continuation, in combination with Gauss collocation to represent orbit segments as piecewise-polynomials over a pre-specified number of mesh intervals; see [8] for details. Curves in $\widehat{W}^s(\Gamma^+)$ can be computed similarly, but now requiring that the end points of the orbit segments lie along a vector in the stable eigenbundle $E^s(\Gamma^+)$ of the periodic orbit Γ^+. The periodic orbit Γ^+ has positive Floquet multipliers and, thus, $W^s(\Gamma^+)$ is orientable and (locally near Γ^+) a topological cylinder. Hence, $W^s(\Gamma^+)$ has two sides (which are joined at Γ^+) and the intersection set of each side needs to be computed separately. Finally, we remark that $\widehat{W}^s(\Gamma^-)$ need not be computed separately, since it is simply the image of $\widehat{W}^s(\Gamma^+)$ under the symmetry (2).

The fact that $\widehat{W}^s(\mathbf{0})$ is a closed curve on S_R for $1 < \varrho < \varrho_{\rm hom}$ follows from the fact that this curve has been computed by a single continuation, during which the angle variable of the ellipse changes over 2π. On the other hand, for $\varrho_{\rm hom} < \varrho < \varrho_{\rm het}$ the sets $\widehat{W}^s(\mathbf{0})$ and $\widehat{W}^s(\Gamma^+)$ are much more complicated: every accurate representation consists of many individual curves segments on S_R. Since it is impractical to start many hundred individual computations of curves, we take the following approach. We still perform a single continuation where the angular variable of the ellipse changes over 2π. However, we must now allow the end point of the orbit segment to leave the sphere S_R when the integration time of the orbit segments becomes too large. This can be achieved by requiring that

$$(T_{\rm max} - T)\,(R - r) = \varepsilon. \tag{A.1}$$

Here r is the distance of the begin point of the orbit segment from the centre of S_R and T is the associated (positive) integration time to the end point near $\mathbf{0}$; the fixed constant $T_{\rm max}$ is a preset maximum integration time during the computation and ε is chosen small (10^{-3} in our computations). Hence, (A.1) describes a hyperbola that switches fast but smoothly between the two competing conditions that $r \approx R$ and that $T \approx T_{\rm max}$. Hence, when T is well below $T_{\rm max}$ then the begin point of the orbit segment lies on S_R to very good accuracy. On the other hand, when $T \approx T_{\rm max}$ then the product (A.1) being kept constant at ε means that r decreases. In this way, the begin point may pass through the interior of S_R during the computation, until again $T < T_{\rm max}$ and the begin point reaches S_R again (meaning that

$r \approx R$). A post-processing step removes the curve segments in the interior of S_R to isolate the several hundred individual curve segments that constitute the approximations of $\widehat{W}^s(\mathbf{0})$ and $\widehat{W}^s(\Gamma^+)$, respectively. The larger $T_{\max}$ is chosen the more curve segments are generated in this way; in fact, the number of curves appears to grow exponentially with $T_{\max}$.

Note that computing the (hundreds of) curve segments presented in this paper required considerable continuation runs that produced several gigabytes of data. We remark that such computations of solution families of BVPs are highly accurate indeed [8, 27]. This is evidenced, in particular, by Fig. 6(d): the three sets of many hundreds of curve segments shown in this figure align perfectly without intersecting each other, in spite of the fact that they were computed in separate continuation runs.

References

[1] V. S. Afrajmovich, V. V. Bykov and L. P. Sil'nikov, The origin and structure of the Lorenz attractor (in Russian), Dokl. Akad. Nauk SSSR 234(2) (1977) 336–339.

[2] P. Aguirre, E. J. Doedel, B. Krauskopf and H. M. Osinga, Investigating the consequences of global bifurcations for two-dimensional invariant manifolds of vector fields, Discrete and Continuous Dynamical Systems – Series A 29(4) (2011) 1309–1344.

[3] H. W. Broer and F. Takens, "Dynamical Systems and Chaos," Applied Mathematical Sciences 172, Springer-Verlag, New York, (2011).

[4] X. Chen, Lorenz Equations Part I: Existence and Nonexistence of Homoclinic Orbits SIAM J. Math. Anal. 27(4) (1996) 1057–1069.

[5] X. Chen, Lorenz equations part II: "randomly" rotated homoclinic orbits and chaotic trajectories Discr. Contin. Dynam. Syst. 2 (1996) 121–140.

[6] X. Chen, Lorenz equations part III: Existence of hyperbolic sets IMA Preprint Series (1995) # 1354.

[7] R. L. Devaney, Knaster-like continua and complex dynamics, Ergodic Theory and Dynamical Systems 13(4) (1993) 627–634.

[8] E. J. Doedel, Lecture notes on numerical analysis of nonlinear equations, in "Numerical Continuation Methods for Dynamical Systems", B. Krauskopf, H. M. Osinga and J. Galán-Vioque (Eds.), Underst. Complex Syst., Springer-Verlag, New York, 2007, pp 1–49.

[9] E. J. Doedel, with major contributions from A. R. Champneys, T. F. Fairgrieve, Yu. A. Kuznetsov, B. E. Oldeman, R. C. Paffenroth, B. Sandstede, X. J. Wang, and C. Zhang. AUTO-07P: Continuation and bifurcation software for ordinary differential equations; available at `http://cmvl.cs.concordia.ca/`.

[10] E. J. Doedel, B. Krauskopf and H. M. Osinga, Global bifurcations of the Lorenz manifold, Nonlinearity 19 (2006) 2947–2972.

[11] Z. Galias and P. Zgliczynski Computer assisted proof of chaos in the Lorenz equations Physica D 115 (1998) 165-188.

[12] P. Glendinning and C. Sparrow, Local and global behavior near homoclinic orbits, J. Statist. Phys. 35 (1984) 645–696.

[13] J. Guckenheimer and P. Holmes, "Nonlinear Oscillations, Dynamical Systems and Bifurcations of Vector Fields," 2^{nd} edition, Springer-Verlag, New York/Berlin, 1986.

[14] J. Guckenheimer and R. F. Williams, Structural stability of Lorenz attractors, Publ. Math. IHES 50 (1979) 59–72.

[15] A. Gutek, On compact spaces which are locally Cantor bundles, Fund. Math. 108 (1980) 27–31.

[16] A. Gutek and J. van Mill, Continua that are locally a bundle of arcs, Topology Proceedings 7 (1982) 63–69.

[17] B. Hassard and J. Zhang, Existence of a homoclinic orbit of the Lorenz system by precise shooting, SIAM J. Math. Analysis 25(1) (1994) 179–196.

[18] B. Hassard, J. Zhang, S. P. Hastings and W. C. Troy, A computer proof that the Lorenz equations havechaotic solutions , Appl. Math. Letters 7(1) (1994) 79–83.

[19] S. P. Hastings and W. C. Troy, A shooting approach to the Lorenz equations Bulletin AMS 27 (1992) 298–303.

[20] A.J. Homburg, Global aspects of homoclinic bifurcations of vector fields, AJ Homburg Memoirs of the AMS 578 (1996) 1–128.

[21] A. J. Homburg and B. Sandstede, Homoclinic and heteroclinic bifurcations in vector fields in "Handbook of Dynamical Systems, Volume 3," H. W. Broer, F. Takens and B. Hasselblatt (Eds.), North-Holland, Amsterdam, 2010, pp 379–524.

[22] E. A. Jackson, The Lorenz system: I. The global structure of its stable manifolds Physica Scripta 32(5) (1985) 469–475.

[23] E. A. Jackson, The Lorenz system: II. The homoclinic convolution of the stable manifolds Physica Scripta 32(5) (1985) 476–481.

[24] J. L. Kaplan and J. A. Yorke, Preturbulence: A regime observed in a fluid flow model of Lorenz, Commun. Math. Phys. 67 (1979) 93–108.

[25] J. Kennedy, How Indecomposable Continua Arise in Dynamical Systems, Annals of the New York Academy of Sciences 704 (1993) 180–201.

[26] B. Krauskopf and H. M. Osinga, Computing geodesic level sets on global (un)stable manifolds of vector fields, SIAM J. Appl. Dyn. Sys. 2 (2003) 546–569.

[27] B. Krauskopf and H. M. Osinga, Computing invariant manifolds via the continuation of orbit segments, in "Numerical Continuation Methods for Dynamical Systems", B. Krauskopf, H. M. Osinga and J. Galán-Vioque (Eds.), Underst. Complex Syst., Springer-Verlag, New York, 2007, pp 117–154.

[28] B. Krauskopf, H. M. Osinga, E. J. Doedel, M. E. Henderson, J. Guckenheimer, A. Vladimirsky, M. Dellnitz and O. Junge, A survey of methods for computing (un)stable manifolds of vector fields, Internat. J. Bifur. Chaos Appl. Sci. Engrg. 15 (2005), 763–791.

[29] E. N. Lorenz, Deterministic nonperiodic flows, J. Atmosph. Sci. 20 (1963) 130–141.

[30] K. Makino and M. Berz, Suppression of the wrapping effect by Taylor model-based verified integrators: long-term stabilization by preconditioning Int. J. Differential Equations and Applications 10 (2005) 353–384.

[31] K. Makino, A. Wittig, M. Berz, S. Newhouse and Y. Zou, Computer assisted proof of chaoticity of the Lorenz system for large ranges of parameters presented at SciCADE 2011; and personal communication with M. Berz.

[32] M. Messias, Dynamics at infinity and the existence of singularly degenerate heteroclinic cycles in the Lorenz system J. Physics A 42 (2009) 115101.

[33] K. Mischaikow and M. Mrozek, Chaos in the Lorenz equations: a computer assisted proof Bulletin AMS 32(1) (1995) 66–72.

[34] K. Mischaikow and M. Mrozek, Chaos in the Lorenz equations: a computer assisted proof part II: Details Mathematics of Computation 67(223) (1998) 1023–1046.

[35] K. Mischaikow, M. Mrozek and A. Szymczak, Chaos in the Lorenz equations: a computer assisted proof part III: Classical parameter values J. Diff. Equations 169 (2001) 17–56.

[36] S. Newhouse, Nondensity of axiom A(a) on S^2, "Global Analysis" (Proc. Sympos. Pure Math., Vol. XIV, Berkeley, Calif., 1968) Amer. Math. Soc., Providence, R.I., 1970, pp 191–202.

[37] J. Palis and F. Takens, "Hyperbolicity & sensitive chaotic dynamics at homoclinic bifurcations," Cambridge University Press, Cambridge, 1993.

[38] Perelló C 1979 Intertwining invariant manifolds and Lorenz attractor in "Global theory of dynamical systems" (Proc. Internat. Conf., Northwestern Univ., Evanston, Ill., 1979), Lecture Notes in Math. **819**, (Berlin: Springer-Verlag), pp. 375–378.

[39] D. Rand, The topological classification of Lorenz attractors, Math. Proc. Cambridge Philos. Soc. 83 (1978) 451–460.

[40] D. Ruelle and F. Takens, On the nature of turbulence, Commun. in Math. Phys. 20(3) (1971) 167–192.

[41] M. A. F. Sanjuán, J. Kennedy, E. Ott and J. A. Yorke, Indecomposable continua and the characterization of strange sets in nonlinear dynamics, Phys. Rev. Lett. 78(10) (1997) 1892–1895.

[42] C. Sparrow, "The Lorenz Equations: Bifurcations, Chaos and Strange Attractors," Appl. Math. Sci. No. 41, Springer-Verlag, New York, 1982.

[43] W. Tucker The Lorenz attractor exists, Comptes Rendus de l'Académie des Sciences Série I. Mathématique 328(12) (1999) 1197–1202.

[44] M. Viana, What's new on Lorenz strange attractors? Math. Intelligencer 22(3) (2000) 6–19.

[45] R. F. Williams, The structure of Lorenz attractors, Publ. Math. IHES 50 (1979) 101–152.

[46] J. A. Yorke and E. D. Yorke, Metastable chaos: The transition to sustained chaotic behavior in the Lorenz model, J. Stat. Phys. 21 (1979) 263–277.